Japanese Journal of Applied Physics

REGULAR PAPER

The preparation of MnO_2-doped $NaNbO_3$-based lead-free ceramics with enhanced energy storage performance and attractive electrocaloric effect

Japanese Journal of Applied Physics **61**, SB1028 (2022) **REGULAR PAPER**
https://doi.org/**10.35848/1347-4065/ac25db**

The preparation of MnO_2-doped $NaNbO_3$-based lead-free ceramics with enhanced energy storage performance and attractive electrocaloric effect

Tao Zhang, Tomoaki Karaki*, and Tadashi Fujii

Department of Intelligent Systems Design Engineering, Faculty of Engineering, Toyama Prefectural University, Imizu, Toyama 939-0398, Japan

*E-mail: chen@pu-toyama.ac.jp

Received July 25, 2021; revised August 25, 2021; accepted September 9, 2021; published online January 28, 2022

MnO_2-doped $0.955NaNbO_3$-$0.045La(Nb_{1/3}Mg_{2/3})O_3$ ceramics were prepared through a conventional method. The effects of MnO_2 amount on the dielectric property, and the phase transition behavior and energy storage performance were studied. The introduction of MnO_2 can obviously improve sintering performance and effectively stabilize anti-ferroelectric phase, accompanied with the variation of phase transition temperature. An enhanced recoverable energy storage density of 2.63 J·cm^{-3} with efficiency of 66.8% was obtained at RT when 1.5% MnO_2 was applied. This sample also demonstrated attractive thermal stability in energy storage from 30 °C–90 °C. In addition, the coexistence of positive and negative electrocaloric effect was observed due to the emergence of anti-ferroelectric phase. A further advantage of the thermal hysteresis phenomenon possesses abilities to enhance dielectric and energy storage properties. This will contribute to the promotion of $NaNbO_3$-based lead-free dielectric capacitors. © 2022 The Japan Society of Applied Physics

1. Introduction

Nowadays, with the soaring development and extensive applications of pulsed power technology, the exploration of energy storage devices has become more prominent in recent years.[1)] Ceramic-based dielectric capacitors hold a dominant position with regard to higher power density (>10^8 W·kg^{-1}) and extremely fast charge-discharge speed (ms or μs) compared to fuels, batteries and supercapacitors.[1–3)] In addition, superior mechanical and thermal stability enable these capacitors to develop into vital energy storage elements of advanced pulsed power techniques.[4,5)] Generally speaking, charge energy density W, recoverable energy density W_{rec} and energy storage efficiency η of ceramic-based dielectric capacitors can be calculated through the integral of P-E hysteresis loops using the following equations:[6,7)]

$$W = \int_0^{P_{max}} E\, dP, \tag{1}$$

$$W_{rec} = \int_{P_r}^{P_{max}} E\, dP, \tag{2}$$

$$\eta = \frac{W_{rec}}{W} \times 100\%, \tag{3}$$

where E, P_r and P_{max} are the external electric field, remnant polarization and maximum polarization, respectively. Anti-ferroelectric (AFE) and relaxor-ferroelectric (RFE) ceramics are superior to others due to the progressive W_{rec} and η resulting from lower P_r, higher P_{max} and moderate breakdown electric field strength (E_b). However, the great majority are $PbZrO_3$ (PZ)-based materials with excellent achievement, especially (Pb, La)(Zr, Ti)O_3 and Pb(Nb, Mg)O_3 systems.[8–12)] The Pb content of PZ-based ceramics usually exceeds 60%, which causes environmental deterioration and human health hazards, presenting serious drawbacks. Therefore, lead-free ceramic-based dielectric capacitors with enhanced energy storage capacity are urgently needed.

For lead-free ceramic capacitors, large P_r, small P_{max} and low E_b will hinder the improvement of W_{rec}.[13,14)] Furthermore, η should also be emphasized, as lower η implies more electricity being converted to heat during the application process, resulting in a reduction in energy storage performance and breakdown of the capacitors.[15)] In recent years, $NaNbO_3$ (NN)-based ceramics have been thoroughly investigated in order to partly replace lead-based materials because of their anti-ferroelectricity and relatively high polarization (30 μC·cm^{-3}).[16–18)] However, existing metastable ferroelectric (FE) phase leads to the appearance of square-shaped P-E loops in polycrystalline NN ceramics at RT.[17)] Therefore, different approaches have been applied to induce AFE phase in NN matrix, especially chemical modification.[19–21)] It is well known that certain compounds can effectively reduce P_r and enhance E_b simultaneously, which improves energy storage properties.[22)]

Usually, high W_{rec} of lead-free ceramics is always induced by the application of large electric field, which depends on some factors including the existence of second phase, grain size and porosity.[23,24)] Thus, apart from chemical modification, sintering aids are attractive to improve electrical properties, which can decrease sintering temperature to inhibit the volatility of alkaline elements, such as MnO_2,[25,26)] CuO[27,28)] and NiO.[29,30)] MnO_2 is not only an effective sintering aid for densification, but an acceptor dopant for improving electrical properties.[31)]

It is well known that La^{3+} can effectively induce AFE phase and decrease the switching field for lead-based materials, accompanied with an increase in E_b.[32)] Similar to this case, La_2O_3 is an often-employed additive for lead-free ceramics to induce phase transition and improve electrical properties.[33,34)] Therefore, in our study, MnO_2-doped $0.955NaNbO_3$-$0.045La(Nb_{1/3}Mg_{2/3})O_3$ lead-free bulk ceramics based on our previous study were fabricated through a conventional solid-state method. The influence of MnO_2 on sintering, phase transition and energy storage performance was investigated.

2. Experimental procedures

The $0.955NaNbO_3$-$0.045La(Nb_{1/3}Mg_{2/3})O_3$-$100xMnO_2$ ($x = 0$, 0.005, 0.010, 0.015, 0.020 in mole ratio) ceramics, abbreviated as $100xMnO_2$, were prepared through a conventional solid-state method. The chemical reagents Na_2CO_3 (99.0%), La_2O_3 (99.9%), MgO (99.99%), Nb_2O_5 (99.9%) and MnO_2 (99.99%) were applied as raw materials. All materials were

baked at 120 °C for at least 24 h to remove absorbed water. The stoichiometric powders were mixed by planetary ball milling with ethanol and zirconia balls for 6 h. The calcination processes were operated at 900 °C–950 °C for 4 h under air atmosphere after mixed slurry was dried and pressed into disks with a diameter of 50 mm. Then, the second ball milling was carried out for 24 h with zirconia balls in ethanol media. Dry powders were pressed into circular disks with 12 mm in diameter under unidirectional pressure of 170 MPa with about 0.5% polyvinyl alcohol (PVA) as binders. Lastly, the green disks were sintered at 1190 °C–1280 °C for 4 h under air atmosphere after PVA was exhausted at 550 °C.

The density was established using the Archimedes method. X-ray diffraction (XRD; Model RINT 2200; Rigaku Smart Lab) analysis with Cu-Kα radiation was carried out to analyze the crystalline structure, in which a parallel X-ray beam method was employed to minimize error factors. Fine powders were used for XRD measurement and pseudo-cubic indication was employed in this study. The surfaces of sintered ceramics were observed by scanning electron microscopy (SEM; S-3000N; Hitachi). The temperature dependent dielectric constant and loss were measured during both heating and cooling processes separately in a temperature range of 25 °C–450 °C. Silver-coated samples with 0.8 mm in thickness were used for this purpose. Using a different process, the ceramics used for *P-E* measurements were polished to 0.15 mm in thickness, and gold electrodes with a diameter of 1.3 mm were plated by vacuum evaporation.

3. Results and discussion

As a sintering aid, MnO_2 can sharply decrease sintering temperature due to the formation of eutectic liquid phase, as shown in Fig. 1, where the optimum sintering temperature decreased obviously from 1280 °C to 1210 °C. Although extra MnO_2 was added, the density was basically unchanged, while the relative density showed a gradual increase due to the lower theoretical density measured by XRD data. This may be caused by the imbalance of ion ratio and charge in the crystal lattice, because Mn^{4+} may diffuse into the crystal lattice and partly replace B-site ions. As a result, the relative density of all samples exceeded 98%, which was beneficial to the electrical properties.

In Fig. 2, the microstructure and particle size distribution are displayed. All specimens were well densified with only a few pores, and homogeneous microstructure with regular

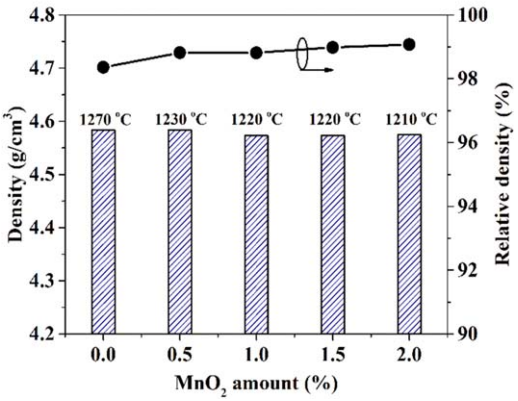

Fig. 1. (Color online) Density and relative density of MnO_2-doped ceramics.

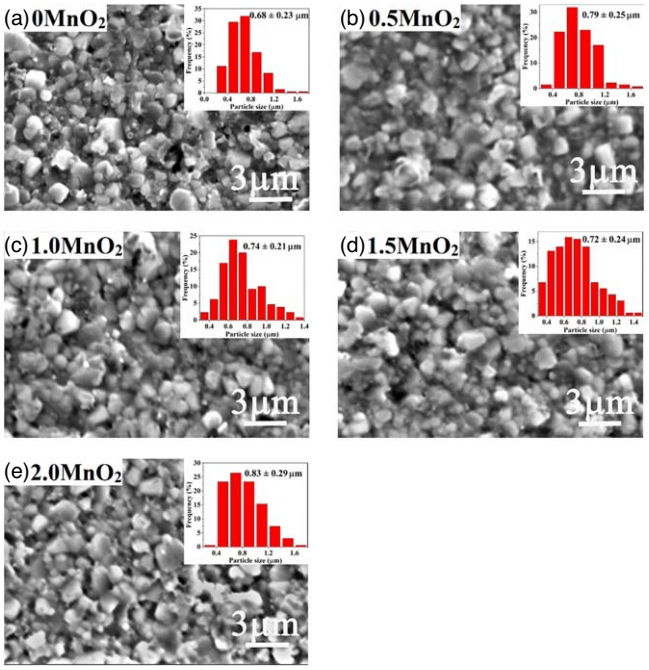

Fig. 2. (Color online) Microstructure and particle size distribution of MnO_2-doped ceramics for (a) $0MnO_2$, (b) $0.5MnO_2$, (c) $1.0MnO_2$, (d) $1.5MnO_2$ and (e) $2.0MnO_2$.

grain was observed, resulting in the enhancement of electrical properties. A slight increase in grain size took place with the addition of MnO_2 because the liquid medium enhanced atomic mobility. However, all samples possessed relatively small particles (<1 μm), which contributed to the improvement in E_b.

XRD patterns of MnO_2-doped ceramics are exhibited in Fig. 3, in which pure perovskite structures without any appreciable secondary phase are observed in all samples. Furthermore, the magnified sections of (200)pc reflection peaks demonstrated passivated singlet, indicating a phase transition from the coexistence of orthorhombic (O) and rhombohedral (R) phase to pure R phase occurred, which was mainly induced by $La(Nb_{1/3}Mg_{2/3})O_3$ (LNM). The introduction of MnO_2 induced no other apparent phase transition, and the mixed phase structure may be beneficial to improve energy storage properties through phase transition. As shown in Fig. 3(b), the location of (200)pc peaks varied slightly with the extension of MnO_2, indicating that Mn^{4+} can partially diffuse into original lattice. Based on a few researches, some of the Mn^{4+} ions can be reduced to Mn^{3+} ions stably at high temperatures of 1100 °C–1200 °C.[25] The ionic radius of Mn^{4+} (0.53 nm CN = 6) and Mn^{3+} (0.65 nm CN = 6) indicated that the dopants were suitable for B-site substitution. The replacement of Nb^{5+} (0.64 nm CN = 6) and Mg^{2+} (0.72 nm CN = 6) led to a movement to higher 2θ angles. However, the diffraction peaks shifted to lower angles in $2.0MnO_2$ ceramics, implying that more additives remained in the grain boundaries and there was a limited amount for extra addition. A close view of XRD spectra around 36.5° and 55.2°, which corresponded to the (11 3/4) and (21 3/4) AFE superlattice diffraction, respectively,[35] is displayed in Figs. 3(c) and 3(d). The intensity of characteristic AFE superlattice peaks was slightly enhanced, which meant that the AFE phase was stabilized by the introduction of MnO_2.

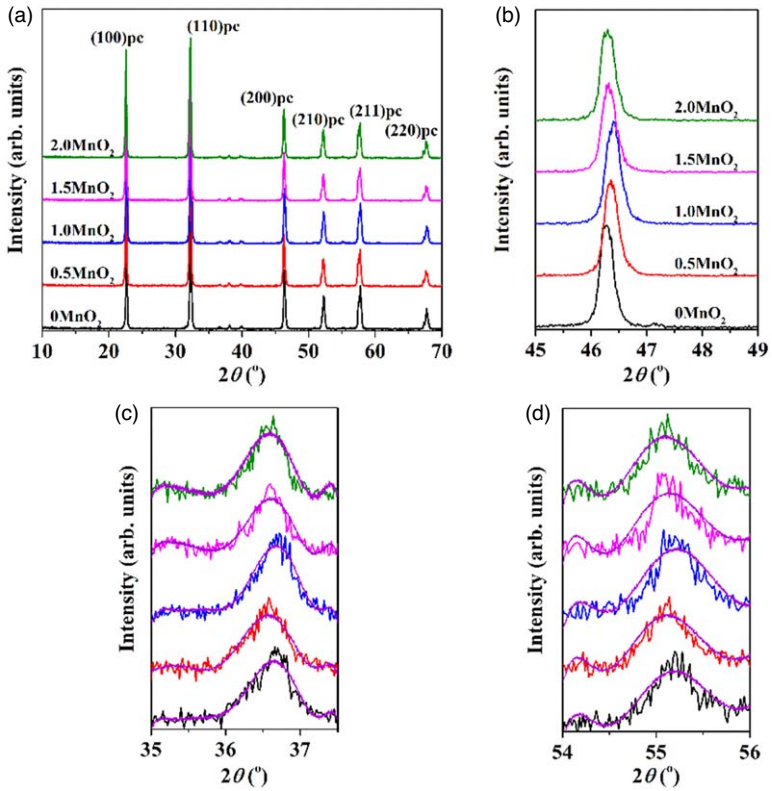

Fig. 3. (Color online) XRD patterns of MnO_2-doped ceramics for (a) 10°–70°, (b) 45°–49°, (c) (11 3/4) AFE superlattice diffraction and (d) (21 3/4) AFE superlattice diffraction.

The dielectric constant (ε_r) and loss ($tan\delta$) of MnO_2-doped ceramics as functions of temperature are demonstrated in Fig. 4. Both heating and cooling measurement sweeps were applied in a temperature range of 25 °C–450 °C. An obvious thermal hysteresis phenomenon was observed in ε_r and $tan\delta$, which was responsible for the first-order AFE-to-AFE phase transition in NN-based matrix.[36] The phase transitions of the heating and cooling processes were both closely related to MnO_2 content, as shown in Fig. 4 and Table I, indicating that partial Mn^{4+} (Mn^{3+}) successfully diffused into lattice structures, which corresponded with XRD results. First, T_C only showed a slight reduction, while the peak temperature (defined as T_C') during the cooling process decreased sharply with the addition of MnO_2. In addition, the temperature difference (ΔT_C) between T_C and T_C' showed an increase-decrease trend. Second, as the amount of MnO_2 increased, the other peak above T_C was more and more apparent, which was caused by the phase transition between orthorhombic R (Pmnm) and S (Pmnm) phase.[37,38] Consequently, a "hump-shaped" curve was observed in the temperature range of 200 °C–350 °C. In addition, the RT dielectric constant ($\varepsilon_{r(RT)}$) increased sharply with the addition of MnO_2, while $tan\delta$ at RT was relatively low (<1%). Furthermore, none of the samples showed any RFE characteristics, because both T_C and T_C' were independent of measured frequency. The fitting results of modified Curie–Weiss law also evidenced this observation, the diffuseness parameter (γ) was around 1, which deviated from RFE characteristics (γ approached 2). Figure 4(f) displays ε_r and $tan\delta$ as functions of frequency at RT, in the frequency range between 100 Hz–1 MHz, ε_r only showed a slight drop and $tan\delta$ exhibited relatively low values (<3%), demonstrating attractive frequency stability.

The difference between $\varepsilon_{r(RT)}$ before and after the dielectric test increased gradually with the increment in MnO_2 amount due to the reduction in T_C'. It could be predicted that T_C' would soon drop below RT, as illustrated in the inset in Fig. 4(e), and T_C also suddenly decreased below RT. To investigate phase transition behavior and try to explore the addition limit of MnO_2, four parameters of T_C, T_C', $\Delta\varepsilon_r$ and $\Delta\varepsilon_r'$ were introduced:

$$\Delta\varepsilon_r = \varepsilon_{r(max)} - \varepsilon_{r(RT)}, \tag{4}$$

$$\Delta\varepsilon_r' = \varepsilon_{r(max)}' - \varepsilon_{r(RT)}', \tag{5}$$

where, $\varepsilon_{r(max)}$ and $\varepsilon_{r(max)}'$ represent the dielectric constant located at T_C and T_C', respectively; $\varepsilon_{r(RT)}$ and $\varepsilon_{r(RT)}'$ are the RT dielectric constant before and after the testing process, respectively. The para-electric phase could normally be constructed at RT when T_C (T_C') $\leqslant$ 25 °C or $\Delta\varepsilon_r$ ($\Delta\varepsilon_r'$) $\leqslant 0$. Thus, the addition limit was located at that point before the phase structure transformed into para-electric phase. As illustrated in Fig. 5, all parameters decreased evidently with the increment of additive content. Although the fitting result of T_C implied that there may be a further reduction in T_C, analysis of the cooling process showed the opposite result [Fig. 5(a)]. The fitting results of $\Delta\varepsilon_r$ and $\Delta\varepsilon_r'$ revealed that the MnO_2 addition limit was around 2.1% before the sudden drop in T_C, as shown by the blue circles in Fig. 5(b). Beyond this limit (2.1%), para-electric phase would be built up at RT [inset in Fig. 4(e)]. It can be deduced that this phase transition became an irreversible process at RT after the sintering reaction. Considered comprehensively, MnO_2 used to stabilize AFE phase rather than para-electric phase should be controlled within 2%.

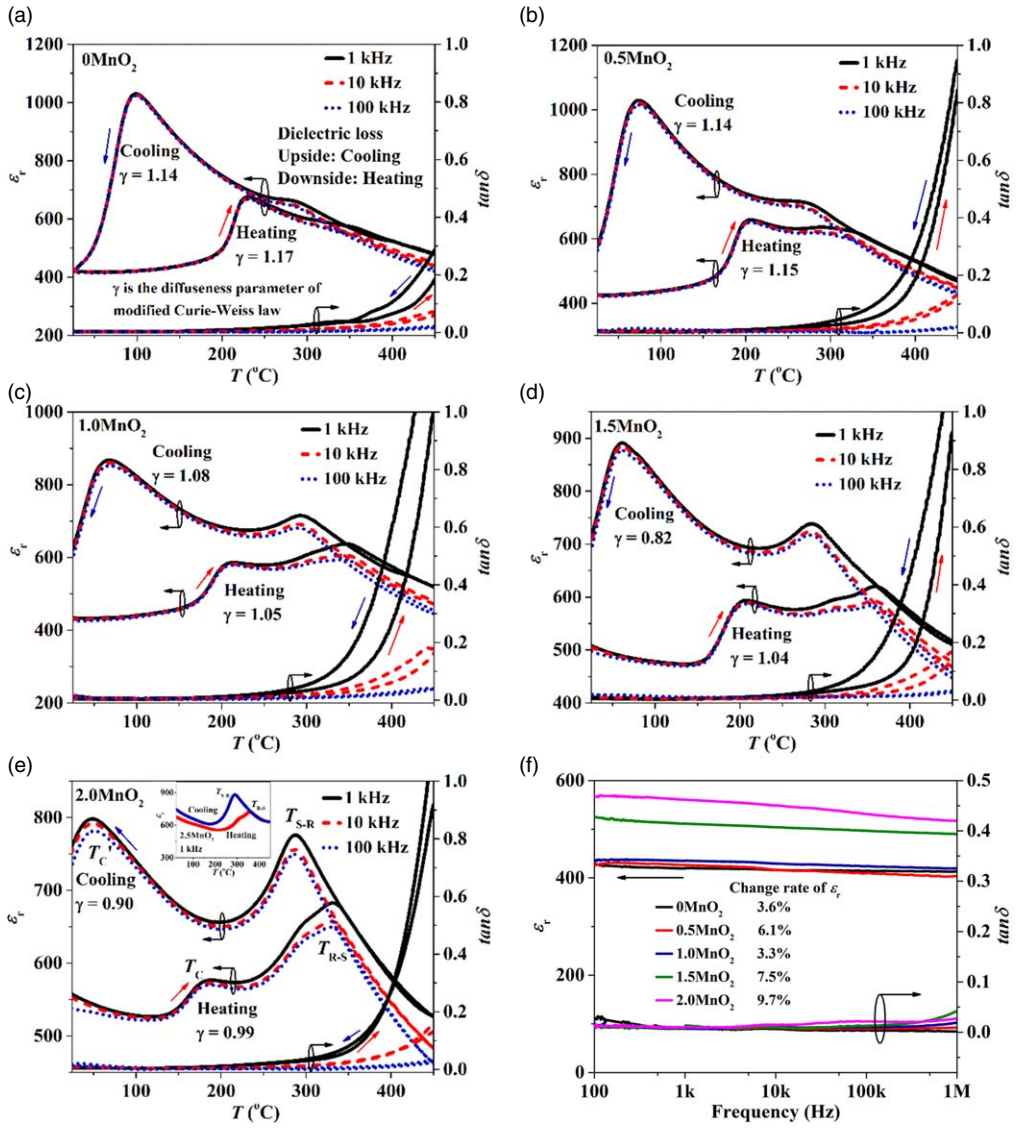

Fig. 4. (Color online) Dielectric properties of MnO_2-doped ceramics for (a)–(e) ε_r-T and $tan\delta$-T curves and (f) ε_r and $tan\delta$ depend on frequency at RT.

Table I. Dielectric properties and phase transition temperatures of MnO_2-doped ceramics.

Sample	T_C (°C)	T_C' (°C)	ΔT_C (°C)	$T_{R\text{-}S}$ (°C)	$T_{S\text{-}R}$ (°C)	$\varepsilon_{r(RT)}$ [a)]	$tan\delta$ [a)] (%)
$0MnO_2$	230	99	131	352	285	419	0.51
$0.5MnO_2$	207	74	133	325	270	425	0.50
$1.0MnO_2$	210	69	141	346	294	434	0.41
$1.5MnO_2$	205	62	143	360	285	508	0.50
$2.0MnO_2$	182	49	133	331	288	557	0.63

a) Measured at RT, 1 kHz.

To confirm the phase transition process, high-temperature XRD measurements of $1.5MnO_2$ and $2.0MnO_2$ were carried out, as displayed in Fig. 6. Although two obvious phase transition peaks were observed in ε_r-T curves, the characteristic (200)pc peaks demonstrated no apparent change with only a single peak was observed. This indicated the phase structure only transformed from the coexistence of O and R phase to cubic structure. The addition of MnO_2 could not trigger more complicated phase transitions, which is consistent with theoretical results and previous conclusions.[35] As the temperature increased, the diffraction peaks gradually shifted to lower angles due to the increase in lattice volume.

Figures 7(a) and 7(b) reveal the P-E loops of MnO_2-doped ceramics measured at 1 Hz and RT. The E_b varied evidently when MnO_2 was added, so all measurements were measured at the optimal electric field rather than an identical one. All P-E loops displayed similar features, manifesting as a relatively slim shape and small P_r. In consideration of frequency-independent dielectric behavior (Fig. 4), the characteristics of P-E loops exhibited the coexistence of AFE and FE phase, which was mainly induced by LNM, and the addition of MnO_2 further stabilized this mixed phase structure. The E_b value increased gradually and then decreased sharply with an increment in MnO_2 amount achieving a maximum value (25.2 kV mm^{-1}) when 1.5% MnO_2 was applied [the inset in Fig. 7(b)]. The variation in P_r and P_{max} demonstrated an interesting phenomenon, which was opposite to the changing law of E_b. Both P_r and P_{max} decreased first with a boost in MnO_2 amount when $x \leqslant 1.5\%$, but larger P_r and P_{max} were obtained in $2.0MnO_2$-doped ceramics, as demonstrated in Fig. 7(c). The reduction in P_r, P_{max} and increase in E_b were normal phenomena induced by additives. However, there were hardly any reports of a sudden increase in P_r, P_{max} and a

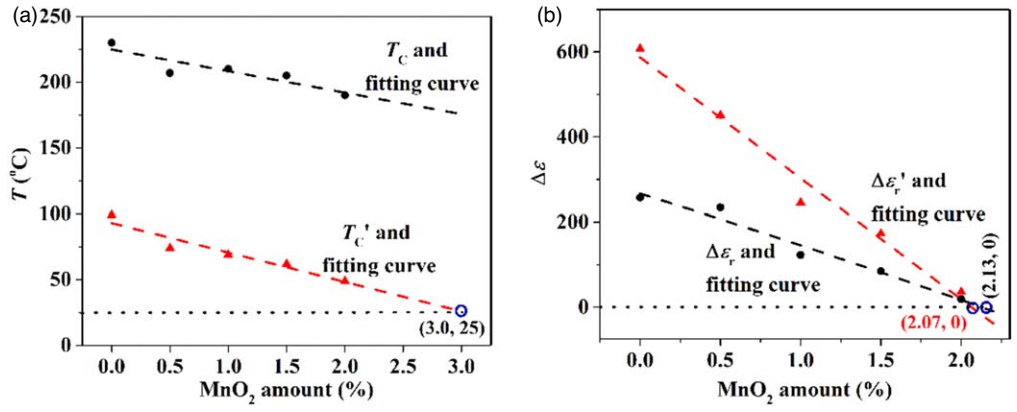

Fig. 5. (Color online) Values and fitting results used to predict the addition limit of MnO_2 for (a) T_C and T_C', (b) $\Delta\varepsilon_r$ and $\Delta\varepsilon_r'$.

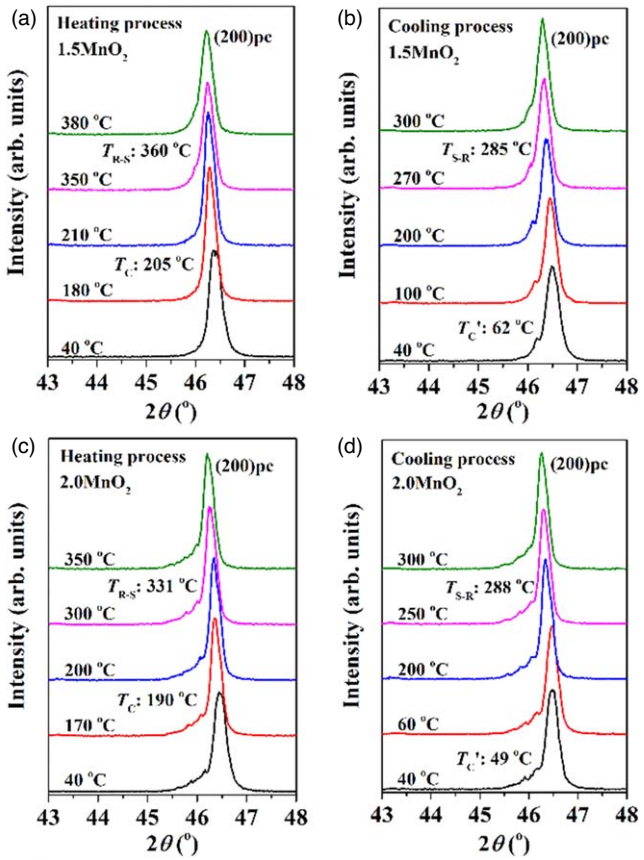

Fig. 6. (Color online) High-temperature XRD patterns during the heating and cooling processes for (a), (b) $1.5MnO_2$ and (c), (d) $2.0MnO_2$.

decrease in E_b. Combined with the analysis of phase transition behavior, we inferred that the phase transition at T_C' (49 °C) should be responsible for this, which was near RT. The 2.0% MnO_2 was much closer to the addition limit (2.1%), which could also be an influence factor. As a result of the significant effect of P_r, P_{max} and E_b, the opposite change trend of W_{rec} and η was observed, as shown in Fig. 7(d). Consequently, an enhanced W_{rec} of 2.63 J·cm^{-3} was obtained at a moderate electric field (25 kV·mm^{-1}) in $1.5MnO_2$, which was much higher than the non-doped ceramics, with η (66.8%) only showing a slight decrease. Furthermore, the W_{rec} (2.27 J·cm^{-3}) of $1.0MnO_2$ with $\eta = 68.0\%$ was also attractive. The energy storage performance detected at the same electric field (18.7 kV mm^{-1}) is displayed in Figs. 7(e) and 7(f). Closely related to P_r and P_{max}, W_{rec} decreased obviously as the MnO_2 content increased when $x \leqslant 1.5\%$, and then suddenly increased to the maximum value (1.49 J·cm^{-3}) in $2.0MnO_2$-doped ceramics, while η exhibited the opposite trend. This was caused by the unique phase transition behavior induced by MnO_2.

Figure 8(a) represents the P-E loops of $1.5MnO_2$-doped ceramics measured at 18 kV·mm^{-1} and 1 Hz. The P-E loops widened slightly as the test temperature was raised. However, no ferroelectric feature was observed in the temperature range. As shown in the inset in Fig. 8(b), both P_{max} and ΔP maintained excellent temperature stability during the temperature range of 30 °C–60 °C, and then showed a slight increase from 70 °C. Correspondingly, W_{rec} and η just dropped a little in the temperature range of 30 °C–90 °C, demonstrating relatively excellent temperature stability in terms of energy storage performance. It was inferred that the introduction of Mn^{4+} with different valence and radius could destroy the long-range ferroelectric order and favor the short-range nanopolar regions.[39] Thus, the AFE stability could be enhanced with weak coupling from region to region, limiting the ability to recover metastable long-range dipole orders.[40,41] Although T_C (205 °C) was much higher than RT, W_{rec} and η only reduced by 4.9% and 2.8%, respectively, from 30 °C to 60 °C, which may have resulted from the lower T_C' (62 °C).

The electrocaloric effect (ECE) of ceramics possesses the potential of solid refrigeration, which is favorable for miniaturization and environmental protection. The ECE of $1.5MnO_2$-doped ceramics was studied, defined by isothermal entropy change (ΔS) and reversible adiabatic temperature change (ΔT). Based on the temperature dependence of P-E loops, ΔS and ΔT could be determined through Maxwell's relations:[42]

$$\Delta S = -\frac{1}{\rho}\int_{E_0}^{E_{max}} \left(\frac{\partial P}{\partial T}\right)_E dE, \tag{6}$$

$$\Delta T = -\frac{1}{\rho}\int_{E_0}^{E_{max}} \frac{T}{C_E}\left(\frac{\partial P}{\partial T}\right)_E dE, \tag{7}$$

where ρ is the density of the sintered ceramic, E represents the applied electric field and C_E is the specific heat of ceramics obtained from the literature.[43] The temperature dependence of polarization was constructed from previous branches of P-E loops and the values of $(\partial P/\partial T)_E$ resulted

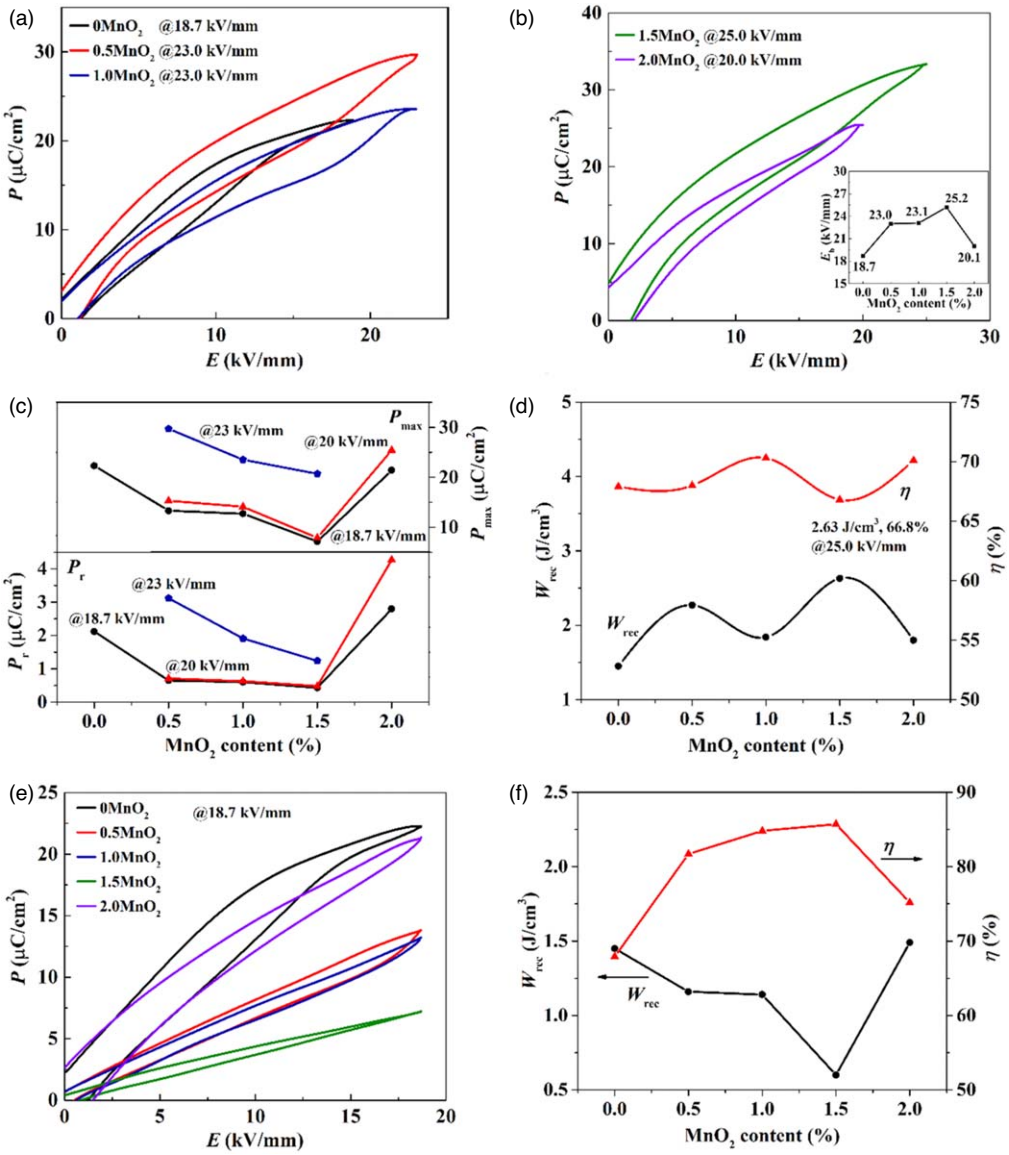

Fig. 7. (Color online) Energy storage performance of MnO_2-doped ceramics for (a), (b) *P-E* loops, (c) P_r and P_{max} values under different electric fields, (d) the calculated W_{rec} and η, (e) *P-E* loops measured at 18.7 kV·mm^{-1} and (f) the calculated W_{rec} and η at 18.7 kV·mm^{-1}.

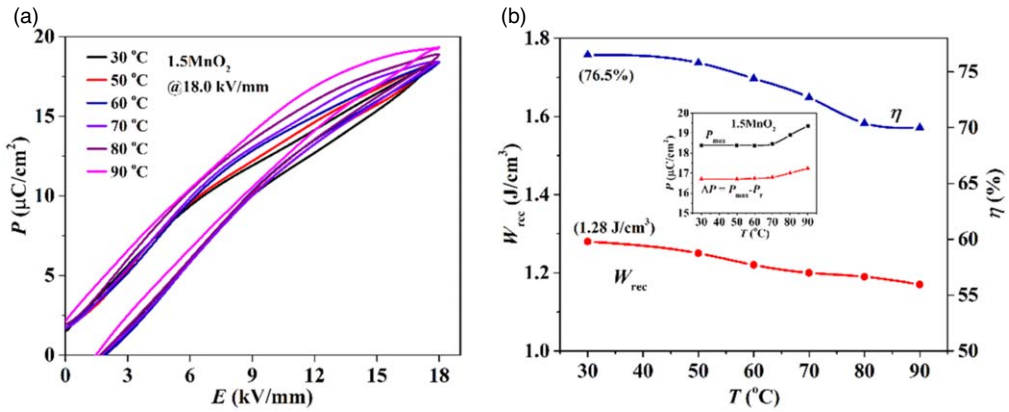

Fig. 8. (Color online) (a) *P-E* loops of $1.5MnO_2$-doped ceramics at different temperatures and (b) the calculated W_{rec} and η values.

from polynomial fitting of *P-T* data were displayed in the inset in Fig. 9(a). Although the maximum entropy change $\Delta S_{max} = 1.38\,J\cdot(K\cdot kg)^{-1}$ and temperature change $\Delta T_{max} = 0.80\,K$ were not excellent, the trend of ΔS and ΔT was attractive. Because the sample possessed positive ECE ($\Delta T > 0$) and negative ECE ($\Delta T < 0$) simultaneously, this could enhance the electrocaloric efficiency.[44] This was caused by the coexistence of FE and AFE phase, and positive and negative ECE were usually observed in FE and AFE materials, respectively.[45] In addition, the transition point of

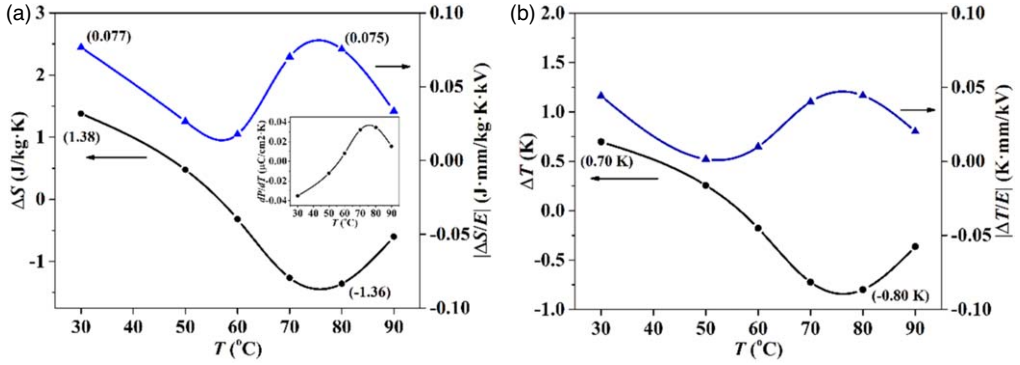

Fig. 9. (Color online) ECE of 1.5MnO_2-doped ceramics for (a) isothermal entropy change (ΔS) and (b) adiabatic temperature change (ΔT).

positive and negative ECE was about 57 °C, close to T_C' (62 °C). The other figure of merit for ECE of the electrocaloric responsivity ($|\Delta T/\Delta E|$) is also displayed in Fig. 9(b).

4. Conclusion

Pure perovskite 0.955$NaNbO_3$-0.045$La(Nb_{1/3}Mg_{2/3})O_3$ ceramics with MnO_2 as additive are successfully prepared through a conventional solid-state method. The optimal sintering temperature is reduced from 1270 °C to 1210 °C with dense microstructure and regular particles by adding MnO_2. The adoption of MnO_2 can stabilize AFE phase and obviously influence the phase transition behavior and thermal stability. Thus, a simple model is constructed to investigate this. Furthermore, the dielectric properties are also improved by the addition of MnO_2, accompanied with a decrease in T_C' from 99 °C to 49 °C, which is close to RT. Enhanced energy storage properties of 1.5MnO_2-doped ceramics are promoted, apparently induced by phase transition with $W_{rec} = 2.63\ J{\cdot}cm^{-3}$ and $\eta = 66.8\%$ at $25\ kV{\cdot}mm^{-1}$. These lead-free bulk ceramics also exhibit relatively admirable thermal stability for energy storage performance, and the coexistence of positive and negative electrocaloric effect is also attractive for solid refrigeration. All presented results illustrate that these lead-free systems are highly promising candidates for applications in electrostatic energy storage devices and pulsed power capacitors.

1) J. H. Seo, Z. M. Fan, H. Nakaya, R. Rajagopalan, E. D. Gomez, M. Iwasaki, and C. A. Randall, Jpn. J. Appl. Phys. **60**, 037001 (2021).
2) S. Rawal, B. Joshi, and Y. Kumar, J. Energy Storage **20**, 418 (2018).
3) M. X. Zhou, R. H. Liang, Z. Y. Zhou, S. G. Yan, and X. L. Dong, ACS Sustain. Chem. Eng. **6**, 12755 (2018).
4) T. M. Correia, M. McMillen, M. K. Rokosz, P. M. Weaver, J. M. Gregg, G. Viola, and M. G. Cain, J. Am. Ceram. Soc. **96**, 2699 (2013).
5) D. P. Shay, N. J. Podraza, N. J. Donnelly, and C. A. Randall, J. Am. Ceram. Soc. **95**, 1348 (2012).
6) W. Wang, Y. P. Pu, X. Guo, R. K. Shi, Y. Shi, M. D. Yang, J. W. Li, X. Peng, and Y. Li, J. Eur. Ceram. Soc. **39**, 5236 (2019).
7) G. Liu et al., Ceram. Int. **45**, 15556 (2019).
8) S. Fukuda, Y. Hashizume, T. Nakajima, and S. Okamura, Jpn. J. Appl. Phys. **57**, 11UF08 (2018).
9) Y. Yang, P. Liu, Y. J. Zhang, K. R. Kandula, J. W. Xu, G. Z. Zhang, and S. L. Jiang, Ceram. Int. **46**, 18106 (2020).
10) L. W. Xu, C. He, X. M. Yang, Z. J. Wang, X. Z. Li, H. N. Tailor, and X. F. Long, J. Eur. Ceram. Soc. **37**, 3329 (2017).
11) Y. Dan, H. J. Xu, K. L. Zou, Q. F. Zhang, Y. M. Lu, G. Chang, H. T. Huang, and Y. B. He, Appl. Phys. Lett. **113**, 063902 (2018).
12) Q. F. Zhang, J. Chen, Y. M. Lu, T. Q. Yang, X. Yao, and Y. B. He, J. Am. Ceram. Soc. **99**, 3853 (2016).
13) T. Q. Shao, H. L. Du, H. Ma, S. B. Qu, J. Wang, J. F. Wang, X. Y. Wei, and Z. Xu, J. Mater. Chem. A **5**, 554 (2017).
14) F. Li, J. W. Zhai, B. Shen, X. Liu, and H. R. Zeng, Mater. Res. Lett. **6**, 345 (2018).
15) F. Yan, H. B. Yang, Y. Lin, and T. Wang, Inorg. Chem. **56**, 13510 (2017).
16) L. E. Cross, Nature **181**, 2 (1958).
17) T. Wada, K. Tsuji, T. Saito, and Y. Matsuo, Jpn. J. Appl. Phys. **42**, 6110 (2003).
18) P. Peng, H. C. Nie, C. Zheng, G. S. Wang, and X. L. Dong, J. Am. Ceram. Soc. **104**, 2610 (2021).
19) K. Beppu, Y. Iida, H. Adachi, I. Fujii, and T. Wada, Jpn. J. Appl. Phys. **58**, SLLB05 (2019).
20) A. W. Xie, H. Qi, and R. Z. Zuo, ACS Appl. Mater. Interfaces **12**, 19467 (2020).
21) T. Wei et al., Ceram. Int. **47**, 3713 (2021).
22) L. T. Yang, X. Kong, Z. X. Cheng, and S. J. Zhang, ACS Appl. Mater. Interfaces **12**, 32834 (2020).
23) X. F. Su, M. Tomozawa, J. K. Nelson, and D. B. Chrisey, J. Mater. Sci., Mater. Electron. **24**, 2135 (2013).
24) A. Young, G. Hilmas, S. C. Zhang, and R. W. Schwartz, J. Am. Ceram. Soc. **90**, 1504 (2007).
25) Y. F. Deng, J. J. Wang, C. X. Zhang, H. Ma, C. G. Bai, D. Q. Liu, F. M. Wu, and B. Yang, Crystals **10**, 705 (2020).
26) N. Wei, T. Karaki, and T. Fujii, Jpn. J. Appl. Phys. **59**, SPPD02 (2020).
27) J. Yoo, Y. W. Lee, and J. Lee, Ferroelectrics **572**, 51 (2021).
28) Y. Y. Liu and T. Morita, Jpn. J. Appl. Phys. **54**, 10ND01 (2015).
29) S. Yotthuan, S. Rueanngam, S. Pinitsoontorn, S. Chootin, and T. Bongkarn, Integr. Ferroelectr. **214**, 56 (2021).
30) Y. Sakai, T. Futakuchi, T. Karaki, and M. Adachi, Jpn. J. Appl. Phys. **53**, 09PB07 (2014).
31) T. Teranishi, S. Azuma, and A. Kishimoto, Jpn. J. Appl. Phys. **58**, SLLC03 (2019).
32) I. V. Ciuchi, L. Mitoseriu, C. Galassi, and G. L. Brennecka, J. Am. Ceram. Soc. **99**, 2382 (2016).
33) Y. Zhang and R. Zuo, J. Eur. Ceram. Soc. **40**, 5466 (2020).
34) T. Tateishi, S. Suzuki, K. Banno, and A. Ando, Jpn. J. Appl. Phys. **58**, SLLC02 (2019).
35) H. Z. Guo, H. Shimizu, Y. Mizuno, and C. A. Randall, J. Appl. Phys. **117**, 214103 (2015).
36) S. K. Mishra, R. Mittal, V. Y. Pomjakushin, and S. L. Chaplot, Phys. Rev. B **83**, 134105 (2011).
37) H. D. Megaw, Ferroelectrics **7**, 87 (1974).
38) S. G. Jabarov, D. P. Kozlenko, S. E. Kichanov, A. V. Belushkin, A. I. Mammadov, B. N. Savenko, R. Z. Mekhtieva, and C. Lathe, J. Surf. Investig. **6**, 546 (2012).
39) M. X. Zhou, R. H. Liang, Z. Y. Zhou, and X. L. Dong, J. Mater. Chem. C **6**, 8528 (2018).
40) L. Zhao, Q. Liu, S. J. Zhang, and J. F. Li, J. Mater. Chem. C **4**, 8380 (2016).
41) H. Ogihara, C. A. Randall, and S. T. McKinstry, J. Am. Ceram. Soc. **92**, 110 (2009).
42) A. S. Mischenko, Q. Zhang, J. F. Scott, R. W. Whatmore, and N. D. Mathur, Science **311**, 1270 (2006).
43) M. Drulis and K. Konieczny, Mater. Sci. Eng. B Solid State Mater. Adv. Technol. **72**, 19 (2000).
44) X. Nie, S. G. Yan, X. F. Chen, S. B. Guo, F. Cao, C. H. Yao, C. L. Mao, X. L. Dong, and G. S. Wang, Phys. Status Solidi A **215**, 1700971 (2018).
45) W. P. Geng, Y. Liu, X. J. Meng, L. Bellaiche, J. F. Scott, B. Dkhil, and A. Q. Jiang, Adv. Mater. **27**, 3165 (2015).